Approaching the limits of cationic and anionic electrochemical activity with the Li-rich layered rocksalt Li3IrO4

Arnaud J Perez, Quentin Jacquet, Dmitry Batuk, Antonella Iadecola, Matthieu Saubanère, Gwenaëlle Rousse, Dominique Larcher, Hervé Vezin, Marie-Liesse Doublet, Jean-Marie Tarascon

Approaching the limits of cationic/anionic electrochemical activity via a novel Li_3IrO_4 compound

Arnaud J. Perez[1,2,3], Quentin Jacquet[1,2,3], Dmitry Batuk[1,4], Antonella Iadecola[3,5], Matthieu Saubanère[3,6], Gwenaëlle Rousse[1,2,3], Dominique Larcher[3,7], Hervé Vezin[3,8], Marie-Liesse Doublet[3,6] and Jean-Marie Tarascon[1,2,3,*]

[1]Collège de France, Chimie du Solide et de l'Energie, UMR 8260, 11 place Marcelin Berthelot, 75005 Paris, France
[2]Sorbonne Universités - UPMC Univ Paris 06, 4 Place Jussieu, 75005 Paris, France
[3]Réseau sur le Stockage Electrochimique de l'Energie (RS2E), FR CNRS 3459, France
[4]EMAT, University of Antwerp, Groenenborgerlaan 171, B-2020, Antwerp, Belgium
[5]Synchrotron SOLEIL, L'Orme des Merisiers Saint-Aubin, 91192 Gif-sur-Yvette, France
[6]Institut Charles Gerhardt, CNRS UMR 5253, Université Montpellier, Place E. Bataillon, 34095 Montpellier, France
[7]Laboratoire de Réactivité et Chimie des Solides, UMR CNRS 7314, 33 Rue Saint Leu, 80039 Amiens, France
[8]Université Lille 1, CNRS UMR 8516-LASIR, 59655 Villeneuve d'Ascq, France

Abstract

Progress over the last two decades in positive electrode materials for Li-ion batteries has generated a variety of novel materials. The Li-rich rocksalt oxides Li_2MO_3 (M = 3d/4d/5d transition metal) are especially promising, displaying capacities exceeding 300 mAh/g thanks to the participation of the oxygen non-bonding O(2p) orbitals in the redox process. Understanding the oxygen redox limitations and the role of O/M ratio is therefore crucial for the rational design of materials with improved electrochemical performances. Herein, we push oxygen redox to its limits with the discovery of a new Li_3IrO_4 compound (O/M = 4) which can reversibly uptake and release 3.5 e- per transition metal; the highest capacity ever reported for any positive insertion electrode, via the cumulative activation of cationic and anionic redox processes. By quantitatively monitoring the oxidation process, we demonstrate the material instability against O_2 release upon removal of all Li. Accordingly; we find the fully-delithiated phase to undergo irreversible amorphization producing a new a-IrO_3 phase with a local structure made of threefold connected IrO_6 octahedra. Our results show that the O/M parameter delineates the boundary between the material's maximum capacity and its stability, hence providing valuable insights for further high capacity materials developments.

The Li-ion battery technology, widely used in portable electronics, is getting increasing importance with respect to large volume applications associated with the development of electric vehicles and renewable energy sources. Such a wide interest justifies the flourishing research activities focusing towards the improvement of this technology in terms of performances, sustainability and safety. They enlist research in the various aspects of the cell components including interfaces. Turning to the positive electrode, great hopes are being placed on the design of novel high capacity electrode materials relying on the recent discovery of anionic redox activity in layered Li-rich NMC.[1] Taking advantage of cumulating both cationic and anionic redox processes within the same compound, new materials (Li-Nb-Mn-O, Li-Mn-O) with capacities exceeding 300 mAh/g were isolated.[2,3] However, the asset provided by such staggering capacities is negated by capacity fade upon cycling, sluggish kinetic for the anionic redox process, and/or surface oxygen depletion in Li-rich NMC. While solving these issues is of major importance for practical applications, the aim of this paper is more fundamental and focusses on pushing the limit of anionic redox through the design of a novel electrode material, in order to highlight the trade-off that needs to be found between large extra-capacity and structural stability.

Such a search is presently backed-up by theoretical calculations, and the literature is becoming rich in papers aiming at defining guidelines or indicators to conceptually identify materials showing a Li-driven anionic activity.[4–6] They all agree on the fact that pure oxygen O(2p) states are required at the Fermi level to reach extra-capacities, a situation that can be triggered from the O/M stoichiometry (Figure 1a). However, the role of the M-O covalence and Li/M cationic disorder on the promotion of these O(2p) non-bonding orbitals at the Fermi level is still under debate. By experimentally playing with these parameters, we identified that Li-rich phases, based on 4d (Li_2RuO_3) or 5d (Li_2IrO_3) metals, i.e. with high M-O bond covalence, are more prone to a reversible anionic redox process than 3d metal (Li_2MnO_3) phases.[7,8] Moreover, we showed that such 4d, 5d based compounds are more stable against surface oxygen release than 3d-based Li-rich NMC phases. By exploring various polymorphs of the Li_2MO_3 series, we demonstrated that the anionic process is not solely linked to Li-rich phases having a layered ($Li_{1.2}Ni_{0.13}Mn_{0.54}Co_{0.13}O_2$)[1] or a disordered rock-salt structure ($Li_{1.3}Nb_{0.3}M_{0.4}O_2$ with M = Mn, Fe)[2], but can also occur in fully ordered 3D structures such as β-Li_2IrO_3.[9] Moreover, trying to achieve electrodes with higher capacities, researchers have explored beyond the $LiMO_2$ to Li_2MO_3 phases the Li_3NbO_4-$LiMO_2$ and Li_4MoO_5-NiO solid solutions, with good capacity and cycling at 55°C for $Li_{1.2}Nb_{0.4}Mn_{0.4}O_2$, but no capacity for

compounds with Li/M and O/M ratio higher than 2 and 3 respectively, in particular for Li_3NbO_4 and Li_4MoO_5,[2,10] which are electronic insulators with no d-electrons (Nb^{5+}, Mo^{6+}).

To further probe the effect of increasing the O/M ratio to reach higher anionic extra-capacities, we embarked on a study of Li_3MO_4 compounds in which the transition metal M contains a partially filled d-band. Searching for such materials, we explored the Li-Ir-O ternary phase diagram and discovered, besides the two α and β Li_2IrO_3 polymorphs, a new Li-rich Li_3IrO_4 phase crystallizing in a layered rocksalt structure. Using complementary *in situ* XRD and XAS experiments coupled with *ex situ* EPR, pressure measurements and DFT calculations, we here show that this phase can be either oxidized ("Li_3IrO_4 → IrO_4") or reduced ("Li_3IrO_4 → Li_5IrO_4") and we provide evidence that this amphoteric character is nested in redox processes involving anions on oxidation ($x < 3$) and cations on reduction ($x > 3$).

Results

Li_3IrO_4 was synthesized by a high temperature method from a stoichiometric mixture of Ir and Li_2CO_3 precursors. The obtained black powder was shown to be a single phase as determined by synchrotron X-ray diffraction (XRD). The pattern (Figure 1b) was refined by the Rietveld method using the hexagonal description (space group *R*-3*m*) of layered $LiMO_2$ phases. The cell parameters and atomic positions are reported in Supplementary Table 1. This new Li_3IrO_4 phase, which can also be written as $Li(Li_{1/2}Ir_{1/2})O_2$, has a layered rocksalt oxide structure with oxygen atoms in a cubic close-packed arrangement, and Li and Ir occupying all octahedral sites (Figure 1b). The cations are organized into pure Li layers alternating with mixed Ir/Li layers, in which Ir and Li are randomly distributed. This cationic arrangement is also confirmed by the HAADF-STEM imaging (Figure 1c). It stands between the completely disordered rocksalt oxides which show only a few Bragg reflections, and the completely ordered layered rocksalt oxides, such as Li_3RuO_4[11] and Li_3NbO_4,[2] whose lower symmetry allows the appearance of superstructure peaks.

The electrochemical performance of Li_3IrO_4 was tested vs. Li in Swagelok cells using a galvanostatic cycling mode. When the cell is started on oxidation, the delithiation occurs through a voltage plateau at an average potential of 3.9-4.0 V vs Li^+/Li (Figure 2a). Strikingly, all three Li can be removed from Li_3IrO_4. Bearing in mind that, in both polymorphs of the parent material Li_2IrO_3 the electrochemical oxidation of Ir is limited to Ir^{5+},[8,9] this suggests a large participation of oxygen in the redox activity of the material. On

the subsequent discharge, the voltage profile becomes slopping, with almost 3 Li reinserted down to a lower cutoff of 2.0 V, and it remains as such on the next charge/discharge cycles with a fair reversibility. By lowering the voltage down to 0 V, we observe a continuous voltage decrease till 0.7 V that corresponds to conversion reaction [Li_xIrO_y + (2y-x) Li^+ + (2y-x) $e^- \rightarrow$ Ir + y Li_2O] (Supplementary Figure 1). It is followed by a continuous voltage decay usually associated with the decomposition of electrolyte into a polymeric gel.[12] Owing to the presence of Ir^{5+} in the pristine material we also tested our electrode starting on reduction and found that Li_3IrO_4 can also reversibly intercalate up to 1.7 extra Li (Figure 2a). This occurs through well-defined processes at 1.9 V and 1.8 V in the dQ/dV derivative curve (Supplementary Figure 2), whose shapes are preserved on cycling, indicating a classical insertion/deinsertion process involving the $Ir^{5+} \rightarrow Ir^{4+} \rightarrow Ir^{3+}$ reduction cascade as we will see later. Overall, the redox activity of Li_3IrO_4 spans over almost 5 electrons, but it seems impossible to take advantage of the whole capacity as the oxidation process is partially irreversible due to a large structural modification. In contrast, the cell shows a reversible capacity of nearly 3.5 e^- per transition metal by changing the cycling conditions and limiting the first delithiation to x = 1 in Li_xIrO_4 (Figure 2b) with a good cyclability over the 25 first cycles, the maximum we have tied so far (Supplementary Figure 3). Such a number of electrons reversibly exchanged per transition metals (~ 3.5) stands as a record among all the metallic oxides used as insertion cathode materials. The rich electrochemistry of Li_3IrO_4 therefore represents an excellent opportunity to investigate in depth the concomitant cationic/anionic redox processes and underpin, via an arsenal of characterization techniques, the science beyond them.

The lithiation-delithiation mechanism in Li_3IrO_4 was examined by *in situ* X-ray diffraction. During the cell discharge (Figure 2d), we observed a continuous increase of all cell parameters (Supplementary Figure 4) indicating a solid solution mechanism till $Li_{3.5}IrO_4$, accompanied with an increase of the unit cell volume ($\Delta V/V$ = +4.2%). For x between 3.5 and 4, the peaks do not shift any longer but their intensity decreases at the expense of a new phase which becomes single phase at x = 4. Then a continuous shift of the Bragg peaks up to x = 4.7 is observed, at the exception of the (001) peak showing that the interlayer distance is preserved. The XRD and neutron patterns of the fully reduced $Li_{4.7}IrO_4$ phase (Figure 2f, 2g) were successfully refined by the Rietveld method with a structural model alike the one used for Li_2NiO_2[13] (Supplementary Table 2) with the extra Li lying in tetrahedral sites (Figure 2h) to minimize cationic repulsion. Such sites arise from the shift of the $(Li_{1/2}Ir_{1/2})O_2$ layers which

transforms the cubic close-packed (ABCABC) into an hexagonal close-packed (ABAB) oxygen stacking. This structural transition doubles the number of available sites in the pure Li layers and should theoretically lead to T1-Li_5IrO_4. Our inability to reach this value experimentally (4.7 instead of 5) is most likely nested in the limited Li^+ diffusion as we are approaching the full occupancy of the Li sites. When the cell is subsequently charged, the solid solution process is reversed with a shift of all peaks except (001) to higher angles at a potential of 1.85 V vs. Li^+/Li, consistent with the oxidation of Ir. It is followed by a biphasic process at 2.05 V which directly leads to the original O3 structure without going through the solid solution observed at the beginning of reduction. Overall, the structural transition is reversible, but proceeds via different paths on reduction and oxidation, a feature shared by other insertion compounds.[14]

In situ XRD diffraction patterns were similarly collected on a Li_3IrO_4/Li cell that was started on oxidation (Figure 2c). We initially observe a slight shift of all Bragg reflections towards lower angles up to x = 2, caused by the delithiation of the material, which is followed by a sudden shift toward larger angles and a drastic loss of peak intensity. After removal of 3 Li, the X-ray powder pattern of the fully delithiated phase "IrO_4" is featureless, indicative of its amorphous nature. The large decrease of the interlayer distance at the end of charge (Supplementary Figure 4) indicates that the complete delithiation of the material leads to its structural collapse. Electron diffraction pattern confirms the amorphization of the material, so that only short-range interatomic correlations survive (Supplementary Figure 5), hence explaining the irreversible capacity of the material when delithiated deeper than x = 1. In contrast, we note (Figure 2e) that when the cell charge is limited to x = 1, all Bragg peaks shift back upon discharge to their initial positions via the O3 → T1 transformation, thus unambiguously proving the reversibility of the insertion process over 3.5 e^-.

In light of previous works, oxygen loss may occur on charge in these high capacity electrodes. To check this point, gas pressure analysis was carried out over the first two charge/discharge cycles. As Li_xIrO_4 is initially charged up to x = 1, the pressure remains constant, but increases rapidly as more Li is removed (Figure 3a). From the pressure increase, we can deduce that approximately 0.35 gas molecules are released per Li_3IrO_4 unit formula. Once the first charge is achieved, the pressure does not change any longer upon cycling. The nature of the gases was assessed by DEMS analysis which clearly shows (Figure 3b) that the released gas at x = 1 is mainly O_2 (m/z = 32) with however the detection of minor amounts of CO_2 (m/z = 44) towards the end of the oxidation process. In the hypothesis of a process

enlisting at most 4 e^-/molecule of gas, as it is expected for the O^{2-}/O_2 transformation, this would lead to an irreversible loss of 1.4 e^-, hence a stoichiometry for the charged product closer to IrO_3 rather than IrO_4. Obviously, caution has to be exercised as this approximation does not take into account the CO_2 component.

Another indirect way to measure the oxygen loss for this highly oxidized sample consists in further exploiting the discharge-driven conversion reaction down to 0 V, with the number of uptaken Li (u) in Li_xIrO_y being related to the amount of oxygen y by u = 2y-x. This is possible because we can assume similar 0 V end-products, i.e. Ir nanoparticles embedded into an amorphous Li-based matrix, as confirmed by HAADF-STEM (Supplementary Figure 6). The discharge capacities of the pristine, (x = 3) the partially charged (x = 2 and 1) and fully charged (x = 0) Li_xIrO_y materials are shown in Figure 3c. No differences can be observed between the pristine, x = 1 and x = 2 samples, implying that no oxygen is released upon oxidation. In contrast, the capacity of the fully charged sample is 2 Li lower than that of the pristine material, implying that, upon oxidation, the amorphization of the material proceeds with the release of one oxygen atom per formula unit. To confirm the stoichiometry, the discharge capacity down to 0 V of the amorphous IrO_3 and the crystalline β-IrO_3 obtained by delithiating β-Li_2IrO_3 were compared (Figure 3c).[9] Both samples show exactly the same capacity, confirming our hypothesis. This material will be designated as a-IrO_3 from now on, where letter a refers to its amorphous nature. By using the area difference between the two voltage curves on conversion collected at nearly equilibrium conditions (C/20), we can also deduce the difference in Gibbs free energy and show that the β-IrO_3 polymorph is more stable than the a-IrO_3 polymorph by 57 kJ/mol (Supplementary Figure 7), a value comparable to that found by Delmer *et al*. for RuO_2.[15] Lastly, the lower number of oxygen released obtained by gas measurement (0.35 O_2) as compared to 0.5 O_2 from electrochemistry is most likely due to partial reactivity of O_2 with the electrolyte and/or Csp.

Operando X-ray Absorption Spectroscopy (XAS) at Ir-L_{III} edge was then carried out on three cells (Figure 4a): one for the reduction process (cell A), one undergoing full oxidation (cell B) and the last one to test the reversible 3.5 e^- cycle after activation to x = 1 (cell C). Principal Component Analysis (PCA) and Multivariate Curve Resolution (MCR) methods were used to extract the individual components from the three sets of data (see Methods), as well as the evolution of their relative concentrations during cycling.[16,17] Only 3 components (Figure 4b) are needed to describe the reduction cycle for cell A, each of them corresponding to well-defined Ir local environments that were characterized by fitting the

EXAFS oscillations (Supplementary Table 3 and Supplementary Figure 8). We could then deduce the distortion of the IrO_6 octahedra during the Li insertion process by monitoring Ir-O and Ir-Ir distances (Figures 4c and 4d): both distances increase from the pristine (A1) to the intermediate (A2) and the reduced (A3) components in agreement with the expected reduction of Ir^{5+} to Ir^{4+} and Ir^{3+}. Worth mentioning is the observed symmetry in the discharge/charge insertion process deduced from XAS data that contrasts with the asymmetric one obtained from XRD data. Such a difference is most likely nested in the sensitivity of the XAS technique to detect the oxidation state of Ir that governs local structural changes, in contrast to XRD which spots long range structural modifications, hence enabling to spot O3 to T1 transition which is not reflected on the XAS data.

For the cell started on oxidation (cell B), 5 components are needed (Figure 4b, center) to satisfactorily describe the data because of the irreversibility of the oxidation process. EXAFS analysis for B1 (pristine) and B2 (intermediate on charge) is very straightforward since the same structural model as for components A1 can be used (Supplementary Table 3). In contrast, for the B3 (fully charged), B4 (intermediate on discharge) and B5 (discharged) components, new models that consider both the loss of oxygen and the amorphous nature of the material were necessary. On that basis, satisfactory fits were obtained with the presence of IrO_6 octahedra having a connectivity increasing from 2 to 3 (Supplementary Figure 9) as expected in light of the new stoichiometry of a-IrO_3. Interestingly, by comparing the B1 to B2 components, we observe a slight decrease of the Ir-O distances (Figure 4c) but an increase of the Ir-Ir distances implying that Ir is not oxidized (Figure 4d). Such variations instead correspond to an increased distortion of the IrO_6 octahedra. The average Ir-O distance eventually increases up to 2.06 Å for B5, consistent with a significant reduction of Ir upon discharge.

Lastly, 3 components were satisfactorily used both on charge and discharge to describe the cycling of cell C, hence indicating the reversibility of the process. The most oxidized component (C1) is relatively close to the pristine spectra of the other cells (A1 and B1), whereas the intermediate (C2) and reduced (C3) components show an increase of both Ir-O and Ir-Ir distances, that support the reduction of Ir.

The *operando* XANES data were used to get information on the oxidation state of Ir during cycling via careful monitoring of the intense white line (WL) that overlaps with the Ir L_{III}-edge (Figure 5, inset). This WL probes dipole-allowed 2p-5d transitions and its area is proportional to the number of unoccupied d orbital states for nd materials, as previously

reported.[18] Thus the WL area (Figure 5a) is a better parameter to follow the oxidation or reduction of Ir, than the energy of the WL (Figure 5b) which is more sensitive to local distortion of the IrO_6 octahedra. When starting on reduction (cell A, blue), both the WL energy and area decrease linearly with composition (~0.84 eV/e^- and ~0.15 %/e^- respectively) and vice versa on the following oxidation, with both curves having similar slopes, indicative of a reversible process. More quantitatively, the area of the WL vary by approximately 24 %, which is in good agreement with the 25% decrease in hole population expected from a classical cationic process from Ir^{5+} (d^4) to $Ir^{3.5+}$ ($d^{5.5}$) and predicted from DFT Bader charge analyses (Supplementary Figure 11).

We now focus on the cell started on oxidation (cell B, red) which shows that both the position in energy (Figure 5b) and the area (Figure 5a) of WL slightly increase, prior to stabilize and slowly decrease once ~0.5 Li is removed. Overall this suggests that oxygen is primarily oxidized instead of iridium during the charging process, although the shift observed at the very early stage of charge cannot discard a hint of Ir^{6+}. Indeed, while such a high oxidation state has never been achieved in the Ir-based rocksalt oxides reported so far,[8,9,16] it has already been stabilized in more ionic perovskites.[19,20] To address this question, electronic structure DFT calculations, including full structural relaxations were performed at x = 3, 2 and 1 (Supplementary Table 4 and Supplementary Figure 11). Results show (i) a major contribution of the oxygen states below the Fermi level in the electronic structure of Li_3IrO_4 that confirms the dominant oxygen participation to the redox process below x = 3 and (ii) a limited oxidation of Ir^{5+} accompanied with a significant IrO_6 local distortions below x = 3 that may explain the WL shift in energy. Turning to the subsequent discharge, it shows a non-linear decrease of both the WL position and area, indicating that both iridium and oxygen participate in the reduction process while their effects cannot be easily disentangled.

During the reversible cycling (cell C, black), both the WL area and its position in energy show a non-monotonous evolution, suggesting a larger degree of participation of Ir and O in the lower and higher voltage region, respectively. The extent of Ir oxidation/reduction is definitely lower than observed in cell A in agreement with the EXAFS analysis.

Electron Paramagnetic Resonance (EPR) measurements were then carried out to probe unpaired spins regardless of whether they belong to cationic or anionic species. We should recall here that Ir^{5+} (d^4), Ir^{3+} (d^6) and $(O_2)^{2-}$ are EPR silent species at X band in contrast to Ir^{4+} (d^5), Ir^{6+} (d^3) or $(O_2)^{3-}$ and $(O_2)^-$ species. *Ex situ* samples were measured for different states of

charge/discharge (Figure 6a). As expected, the pristine material, which contains Ir^{5+} (EPR silent) and O^{2-} (diamagnetic), gives no signal (i). In contrast, the EPR spectrum of the fully reduced sample ($Li_{4.7}IrO_4$) shows a broad and anisotropic signal (ii) associated with Ir^{4}+, which can nicely be visualized by plotting the data over the full (0 to 800 mT) scale (Figure 6c). From integration of the EPR signal, we could calculate a density of ca. 0.2 spin/Ir. This would correspond to 20% Ir^{4+} and 80% EPR-silent Ir, most likely Ir^{3+}, a ratio close to that expected from the electrochemical composition $Li_{4.7}IrO_4$.

On oxidation, upon removal of 1 Li (x = 2), an intense isotropic signal appears that can be attributed to oxidized $(O_2)^{3-}$ species (iii). This signal becomes approximately 5 times less intense and more anisotropic (axial symmetry with $g_{//} = 2.012$ and $g_{\perp} = 2.006$) upon removal of 2 Li (iv), suggesting an increasing proportion of more oxidized EPR silent $(O_2)^{2-}$ peroxo species that are known to be highly unstable[4,5] and may recombine into O_2 gas, hence explaining why the EPR spectrum remains alike for a-IrO_3 (v) as oxygen is released. This is corroborated by pressure measurements and DFT calculations both showing the decomposition of Li_xIrO_4 into Li_xIrO_3 + ½ O_2 for $x \leq 1$ (Supplementary Figure 12). The EPR spectra for a Li_3IrO_4 sample fully charged and discharged (vi) having the composition "a-Li_3IrO_3" shows an intense Ir^{4+} signal, with an integrated spin density around 0.5 spin/Ir, corresponding to 50% Ir^{4+} and 50% EPR silent Ir. The signal shape reveals an isotropic character more important than for the sample initially reduced suggesting a more disordered Ir coordination sphere, which is in line with the amorphization and the increased connectivity of IrO_6 octahedra deduced from EXAFS measurement. Lastly, for the sample charged to x = 1 and then discharged to 2.6 and 1.8 V, we note the disappearance of the isotropic $(O_2)^{n-}$ signal (vii) to the expense of a sharp signal characteristic of the carbon (viii), as previously reported,[21] hence indicating the full reduction of peroxo-like species as expected.

Discussion

In this work, we report the design and synthesis of a novel Li_3IrO_4 phase, having an enhanced amount of oxygen non-bonding orbitals compared to Li_2MO_3 structures due to less M-O bonding interactions, and a lower weight per Li of ca. 30% due to a higher O/M ratio. This new phase was shown to reversibly uptake and release 3.5 Li per transition metal, hence dethroning the record of 2.5 Li previously established for β-Li_2IrO_3. This unusually high capacity for insertion cathode materials in Li-ion batteries gives us an opportunity to address important questions about anionic redox. Among them, we discuss (i) the possibility to increase the capacity of materials relying on both cationic and anionic redox, (ii) the limit of

stability of these materials versus degassing and/or loss of their structural integrity and (iii) the strategies to be implemented in the search for new high capacity Li-rich cathode materials based on this knowledge.

It is worth emphasizing that the findings of this work were driven by challenging theoretical predictions that we experimentally verified. Having identified the oxygen lone-pairs in non-bonding O(2p) orbitals as the origin of the anionic redox process, Saubanère *et al.*[4] speculated that greater capacities could be achieved by increasing the number of such O(2p) lone pairs through larger O/M ratio in the rocksalt structure. Bearing in mind that the interaction of Li(1s) with O(2p) orbitals is limited to electrostatic stabilization (i.e. no formation of a covalent bond) the interest in compounds with Li_3MO_4 formula became obvious. Needless to say, that such a direction comes with the risk of increasing the instability of these materials against oxygen recombination/release, hence requiring a careful selection of the transition metal. In that respect, dealing with the network stability of layered rocksalt vs. O_2 release, Xie *et al.*[5] theoretical paper was instructive by i) stating that M-O covalency is required to stabilize the oxygen network and ii) by showing that delithiated rocksalt compounds with 3d metals are fully unstable once Li is removed.[5] Thus, the need to further increase the covalence of our system by exploring the Li_3IrO_4 phase which stands at the edge in terms of stability.

The Li_3IrO_4 phase pushes the anionic redox to its limit. Three Li can indeed be extracted from Li_3IrO_4 upon oxidation without the participation of iridium to the redox process, but such an exacerbated capacity does not come for free since it is accompanied with a loss of oxygen and a complete amorphization of the material at the end of charge. This overall oxidation is rationalized by the decomposition enthalpies of Li_xIrO_4 into Li_xIrO_3 + ½ O_2 computed for different Li contents (x) and showing that Li_xIrO_4 starts to be unstable with respect to O_2 release for values of $x \leq 1$, as experimentally observed. Interestingly, the resulting a-IrO_3 material has the same stoichiometry and structural IrO_6 connectivity as the crystalline β-IrO_3, obtained from the oxidation of β-Li_2IrO_3, which is perfectly stable versus oxygen release. Pushing further the calculations, we found that the decomposition of Li_xIrO_4 into Li_xIrO_3 + ½ O_2 competes with a structural phase transition that converts the IrO_4 framework, made of condensed chains of edge-shared IrO_6 octahedra, into a more opened framework consisting in fully disconnected IrO_4 tetrahedra (Supplementary Figures 12 and 13). Interestingly, this Oh to Td transition not only modifies the Ir environment (Supplementary Table 4) but also stabilizes the oxygen network, which opens new

perspectives to make this transition the winning mechanism over O_2 release. These predictions make the search of stabilizing delithiated Li_xMO_4 structures worth pursuing.

Finally, the possibility to tune the cationic/anionic redox activity of a material by changing the Li/M or O/M ratio represents a great opportunity to prepare new cathode materials as it opens a field previously restricted to layered oxides to the entire family of rocksalt oxides. Furthermore, the vast array of structures existing for the Li_3MO_4 family, exemplified by the $y\,Li_3RuO_4 - (1\text{-}y)\,Li_3NbO_4$ system,[22] opens up a new playground for designing new materials with complex structures. As it was observed for the Li_2IrO_3 system,[9] it can also be interesting to search for tridimensional frameworks in order to improve the structural stability upon cycling. Thus, an inspiration from this work is rooted in the investigation of ordered rocksalt Li_3MO_4 structures with large capacities and based on a well-defined combination of 3d/4d/5d transition metals.

As a whole, these findings once again highlight the richness of the anionic redox chemistry together with its complexity when designing high capacity materials, as there is a subtle balance between increasing the number of oxygen non-bonding orbitals and ensuring the stability of the peroxo-like species against oxygen recombination. Fundamentally-wise, the present findings are pleasant as they fall in line with our cumulated understanding of the anionic redox activity. Looking forward, by further combining this knowledge with chemical considerations, there is also hope of generating high capacity and practical Li-based oxides relying on cationic-anionic redox reactions. Designing materials with increased O/M ratios provides indeed an appealing direction, but we should not get too ambitious since highly oxidized MO_y materials are known to become as less thermodynamically stable as y increases. Obviously, a trade-off would have to be found between extra-capacity and structural stability, both a blessing and a challenge for further studies.

Methods

Material synthesis and characterization

Li_3IrO_4 was prepared by mixing metallic Ir (Alfa Aesar, 325 mesh, 99.9%) and Li_2CO_3 (Sigma Aldrich, 99%) precursors in stoichiometric proportions using a mortar and pestle. The mix was heated in a covered alumina crucible using a muffle furnace by slowly heating in air at 1°C/min up to 950°C, left at this temperature for 24 h, and finally cooled naturally to room temperature. Synchrotron X-ray diffraction measurements were performed on the 11-BM beamline of the Advanced Photon Source at Argonne National Laboratory, with a wavelength of 0.414 Å. Neutron Diffraction (ND) pattern was measured for the reduced material on the D1B powder diffractometer (Institut Laue-Langevin) with a wavelength $\lambda = 1.291$ Å. Diffraction data was refined by the Rietveld method using the hexagonal description of layered $LiMO_2$ phases. The space group, cell parameters and atomic positions are reported in Supplementary Table 1. To prepare the large amount of powder needed for neutron experiment, a large cell was discharged down to 1.3 V and the electrode recovered after being washed. *In situ* XRD measurements were performed using an airtight electrochemical cell equipped with a Be window[23] in a BRUKER D8 Advance diffractometer with Cu Kα radiation ($\lambda_{K\alpha1} = 1.54056$ Å, $\lambda_{K\alpha2} = 1.54439$ Å). Structures of the pristine material and structural transformations upon complete charge/discharge were also analyzed using transmission electron microscopy (TEM). High angle annular dark-field images scanning TEM (HAADF-STEM) images and electron energy loss (EELS) spectroscopy data were acquired on a probe aberration corrected FEI Titan 60-300 microscope. The samples were prepared by dipping holey carbon TEM grids into finely ground powder. Specialized Gatan vacuum transfer holder was used for the analysis.

Electrochemistry

Electrochemical characterization was performed in Swagelok-type cells. The active material was used either as a powder mixed with 20% carbon SP, or as a self-standing electrode prepared by laminating a mixture composed of 5 wt% PTFE, 10 wt% carbon SP and 85 wt% active material. Unless otherwise specified, typical loadings of 10 mg of active materials were used. Metallic lithium was used as the negative electrode and a Whatman GF/D borosilicate glass fiber membrane as the separator. The separator was soaked with LP100 electrolyte (1M $LiPF_6$ in EC:PC:DMC = 1:1:3). The cells were assembled in an Ar-filled glovebox and cycled in galvanostatic mode at rates ranging from C/4 to C/20 (4 to 20 hours/Li^+).

Gas analysis

In situ measurements of pressure evolution in the cell during galvanostatic cycling was done using a Swagelok-derived electrochemical cell equipped with a pressure sensor.[24] After assembling, the cell was left to equilibrate at open circuit voltage (OCV) for 15 h at a controlled temperature of 25°C prior to cycling in order to stabilize the pressure. The cells were then cycled at a rate of C/10 with active material loadings ranging from 5 to 20 mg. Differential electrochemical mass spectrometry (DEMS) measurement were carried out using the same cell, with two additional connections to flush Ar gas in and out to a Hiden Analytical mass spectrometer. The current of all m/z fragments from 1 to 100 were measured and used to normalize individual contributions. For the DEMS experiment, 1 M $LiPF_6$ in PC was used as an electrolyte and the cell was flushed with Ar for several hours before cycling.

X-ray absorption spectroscopy

Operando XAS measurements at the Ir L_{III}-edge were performed in transmission mode at the ROCK beamline[25] of synchrotron SOLEIL (France). A Si (111) channel-cut quick-XAS monochromator with an energy resolution of 2 eV at 11 keV was used. The intensity of the monochromatic X-ray beam was measured by three consecutive ionization detectors. The *in situ* electrochemical cell[23] was placed between the first and the second ionization chambers. Self-standing PTFE films of the active material were used and cycled at C/4. One cell was started on reduction to 1.4 V and charged again (cell A). Another was started on oxidation to 4.8 V and discharged (cell B). For the last measurement, an electrode was precharged in a swagelok cell until x = 1 and discharge to x = 2, before being transferred to the *in situ* cell and cycled reversibly between 1.3 and 4 V (cell C). For each cell, successive spectra were collected at a rate of 2 Hz and averaged out over periods of 5 minutes. The energy calibration was established with simultaneous absorption measurements on an Ir metal foil placed between the second and the third ionisation chamber. The data was treated using the Demeter package for energy calibration and normalization.[26] The normalized spectra were then globally analyzed with Principal Component Analysis (PCA)[16] in order to individuate the orthogonal components able to describe the whole evolution during cycling. The number of principal components was then used as basis for Multivariate Curve Resolution-Alternating Least Squares (MCR-ALS)[17] analysis. Finally, the reconstructed components were fitted using the Artemis software.[26] Fourier transforms of EXAFS oscillations were carried out in k-range from 3.5 $Å^{-1}$ to 16 and 14 $Å^{-1}$ for crystalline and amorphous components, respectively. Fitting was performed in R-range from 1.0 to 3.6 Å using k^3 weight. EXAFS amplitudes and

phase-shifts were calculated by FEFF7 with a starting model derived from the zig-zag chains of Li_3RuO_4 (Supplementary Table 3).[11] Except the radial distance (R) and the Debye-Waller factor (σ^2), all other parameters were kept constant (N_i, E_0, S_0^2) in the conventional least squares modelling using the phase and amplitude factors calculated by the FEFF7. The magnitude of the Fourier transform (FT) of EXAFS oscillations represents the local atomic distribution around the Ir atom (Supplementary Figures 8, 9 and 10). The first peak of FT corresponds to the nearest 6 O atoms sitting at ~ 2 Å (peak at ~1.5 Å), while the second peak is due to the next nearest 2 Ir atoms (peak at ~3 Å). Note that the FTs shown are not corrected for the phase shift. The XANES region close to the White Line (WL) was fitted by using an arctangent function for the edge, with fixed width and height, and a single Gaussian function to fit both the t_{2g} and e_g components of the WL. The position and area of the Gaussian were used to follow the changes in position and area of the WL during cycling. The area was alternatively calculated by subtracting the arctangent function from the experimental data and integrating the area of the peak, as described by Clancy *et al.*,[27] yielding to similar results compared to those of the fitting procedure, with the advantage of being independent of the function chosen to fit the WL.

Electron paramagnetic resonance spectroscopy

Ex situ samples for EPR analysis were recovered in the glovebox after cycling, washed several times with DMC and sealed in high purity quartz capillary. EPR samples were collected at 5 K using a Bruker ELEXYS E580 spectrometer operating at 9 GHz. The spectra were recorded with an amplitude modulation of 2 G and microwave power of 5 mW. Spin concentration of samples was calculated with calibrated weak-pitch sample for organic species and copper sulfate for inorganic ones.

First-Principles DFT calculations

Spin-polarized density functional theory (DFT) calculations were performed using the plane-wave density functional theory VASP (Vienna ab initio simulation package) code[28,29] within the generalized gradient approximation of Perdew−Burke−Ernzerhof (PBE) to describe electron exchange and correlation[30]. The rotationally invariant Dudarev method (DFT + U)[31] was used to correct the self-interaction error of conventional DFT for correlated d-electrons. In the case of the disordered Li_3IrO_4, the zigzag chain structure of Li_3RuO_4[11] was employed as a model structure for the calculation and several configurations were computed for delithiated compounds. The crystal structures, electronic and electrochemical properties of the Li_xIrO_4 phases were performed for different U_{eff} = U − J = 0, 2 and 4 eV for M (J = 1 eV).

References

1. Koga, H. *et al.* Reversible Oxygen Participation to the Redox Processes Revealed for $Li_{1.20}Mn_{0.54}Co_{0.13}Ni_{0.13}O_2$. *J. Electrochem. Soc.* **160,** A786–A792 (2013).
2. Yabuuchi, N. *et al.* High-capacity electrode materials for rechargeable lithium batteries: Li_3NbO_4-based system with cation-disordered rocksalt structure. *Proc. Natl. Acad. Sci.* **112,** 7650–7655 (2015).
3. Freire, M. *et al.* A new active Li-Mn-O compound for high energy density Li-ion batteries. *Nat. Mater.* **15,** 173–177 (2016).
4. Saubanère, M., McCalla, E., Tarascon, J.-M. & Doublet, M.-L. The intriguing question of anionic redox in high-energy density cathodes for Li-ion batteries. *Energy Environ. Sci.* **9,** 984–991 (2016).
5. Xie, Y., Saubanère, M. & Doublet, M.-L. Requirements for reversible extra-capacity in Li-rich layered oxides for Li-ion batteries. *Energy Environ. Sci.* **10,** 266–274 (2017).
6. Seo, D.-H. *et al.* The structural and chemical origin of the oxygen redox activity in layered and cation-disordered Li-excess cathode materials. *Nat. Chem.* **8,** 692–697 (2016).
7. Sathiya, M. *et al.* Reversible anionic redox chemistry in high-capacity layered-oxide electrodes. *Nat. Mater.* **12,** 827–835 (2013).
8. McCalla, E. *et al.* Visualization of O-O peroxo-like dimers in high-capacity layered oxides for Li-ion batteries. *Science* **350,** 1516–1521 (2015).
9. Pearce, P. E. *et al.* Evidence for anionic redox activity in a tridimensional-ordered Li-rich positive electrode β-Li_2IrO_3. *Nat. Mater.* **16,** 580–586 (2017).
10. Yabuuchi, N., Tahara, Y., Komaba, S., Kitada, S. & Kajiya, Y. Synthesis and Electrochemical Properties of Li_4MoO_5–NiO Binary System as Positive Electrode Materials for Rechargeable Lithium Batteries. *Chem. Mater.* **28,** 416–419 (2016).

11. Alexander, A. *et al.* Structural and magnetic properties of Li_3RuO_4. *J. Mater. Chem.* **13,** 2612–2616 (2003).
12. Cabana, J., Monconduit, L., Larcher, D. & Palacín, M. R. Beyond Intercalation-Based Li-Ion Batteries: The State of the Art and Challenges of Electrode Materials Reacting Through Conversion Reactions. *Adv. Mater.* **22,** E170–E192 (2010).
13. Dahn, J. R., von Sacken, U. & Michal, C. A. Structure and electrochemistry of $Li_{1\pm y}NiO_2$ and a new Li_2NiO_2 phase with the $Ni(OH)_2$ structure. *Solid State Ion.* **44,** 87–97 (1990).
14. Moreau, P., Guyomard, D., Gaubicher, J. & Boucher, F. Structure and Stability of Sodium Intercalated Phases in Olivine $FePO_4$. *Chem. Mater.* **22,** 4126–4128 (2010).
15. Delmer, O., Balaya, P., Kienle, L. & Maier, J. Enhanced Potential of Amorphous Electrode Materials: Case Study of RuO_2. *Adv. Mater.* **20,** 501–505 (2008).
16. Massart, B. *et al. Handbook of Chemometrics and Qualimetrics*. (Elsevier, 1997).
17. Juan, A. de, Jaumot, J. & Tauler, R. Multivariate Curve Resolution (MCR). Solving the mixture analysis problem. *Anal. Methods* **6,** 4964–4976 (2014).
18. Qi, B., Perez, I., Ansari, P. H., Lu, F. & Croft, M. L_2 and L_3 measurements of transition-metal 5d orbital occupancy, spin-orbit effects, and chemical bonding. *Phys. Rev. B* **36,** 2972–2975 (1987).
19. Choy, J.-H., Kim, D.-K., Demazeau, G. & Jung, D.-Y. LIII-Edge XANES Study on Unusually High Valent Iridium in a Perovskite Lattice. *J. Phys. Chem.* **98,** 6258–6262 (1994).
20. Choy, J.-H., Kim, D.-K., Hwang, S.-H., Demazeau, G. & Jung, D.-Y. XANES and EXAFS Studies on the Ir-O Bond Covalency in Ionic Iridium Perovskites. *J. Am. Chem. Soc.* **117,** 8557–8566 (1995).
21. Zhu, Z. *et al.* Anion-redox nanolithia cathodes for Li-ion batteries. *Nat. Energy* **1,** 16111 (2016).

22. Jacquet, Q. *et al.* The $Li_3Ru_yNb_{1-y}O_4$ ($0 \leq y \leq 1$) System: Structural Diversity and Li Insertion and Extraction Capabilities. *Chem. Mater.* **29,** 5331–5343 (2017).
23. Leriche, J. B. *et al.* An Electrochemical Cell for Operando Study of Lithium Batteries Using Synchrotron Radiation. *J. Electrochem. Soc.* **157,** A606–A610 (2010).
24. Lepoivre, F., Grimaud, A., Larcher, D. & Tarascon, J.-M. Long-Time and Reliable Gas Monitoring in Li-O_2 Batteries via a Swagelok Derived Electrochemical Cell. *J. Electrochem. Soc.* **163,** A923–A929 (2016).
25. Briois, V. *et al.* ROCK: the new Quick-EXAFS beamline at SOLEIL. *J. Phys. Conf. Ser.* **712,** 012149 (2016).
26. Ravel, B. & Newville, M. ATHENA, ARTEMIS, HEPHAESTUS: data analysis for X-ray absorption spectroscopy using IFEFFIT. *J. Synchrotron Radiat.* **12,** 537–541 (2005).
27. Clancy, J. P. *et al.* Spin-orbit coupling in iridium-based 5d compounds probed by x-ray absorption spectroscopy. *Phys. Rev. B* **86,** 195131 (2012).
28. Kresse, G. & Hafner, J. Ab initio molecular dynamics for liquid metals. *Phys. Rev. B* **47,** 558–561 (1993).
29. Kresse, G. & Furthmüller, J. Efficiency of ab-initio total energy calculations for metals and semiconductors using a plane-wave basis set. *Comput. Mater. Sci.* **6,** 15–50 (1996).
30. Perdew, J. P., Burke, K. & Ernzerhof, M. Generalized Gradient Approximation Made Simple. *Phys. Rev. Lett.* **77,** 3865–3868 (1996).
31. Dudarev, S. L., Botton, G. A., Savrasov, S. Y., Humphreys, C. J. & Sutton, A. P. Electron-energy-loss spectra and the structural stability of nickel oxide: An LSDA+U study. *Phys. Rev. B* **57,** 1505–1509 (1998).

Acknowledgements

We thank P. Pearce for providing the β-Li_2IrO_3 and L. Lemarquis for helping in the DEMS experiment. We are particularly grateful to S. Belin, V. Briois and L. Stievano for helpful discussions on XAS analysis and synchrotron Soleil (France) for providing beamtime at the ROCK beamline (financed by the French National Research Agency (ANR) as a part of the "Investissements d'Avenir" program, reference: ANR-10-EQPX-45). V. Nassif is acknowledged for her help during neutron diffraction experiments performed at Institut Laue Langevin on D1B. Use of the 11-BM mail service of the APS at Argonne National Laboratory was supported by the U.S. Department of Energy under contract No. DE-AC02-06CH11357 and is greatly acknowledged. This work has been performed with the support of the Agence Nationale pour la Recherche (ANR) under contract No. 110201 – DeLi-RedOx.

Author information

Corresponding author: jean-marie.tarascon@college-de-france.fr

Author contributions

A.J.P carried out the synthesis; A.J.P, Q.J., D.L. and J.-M.T. designed and performed the electrochemical studies; A.J.P, Q.J. and G.R. did the diffraction experiments and analysis; A.J.P, Q.J. and A.I. did the X-ray absorption study; D.B. collected and analyzed the TEM images; H.V. collected and analyzed the EPR spectra; M.S. and M.-L.D. conducted the DFT study; A.J.P and J.-M.T. wrote the manuscript and all authors discussed the experiments and edited the manuscript.

Additional information

Supplementary information is available.

Competing financial interests

The authors declare no competing financial interest.

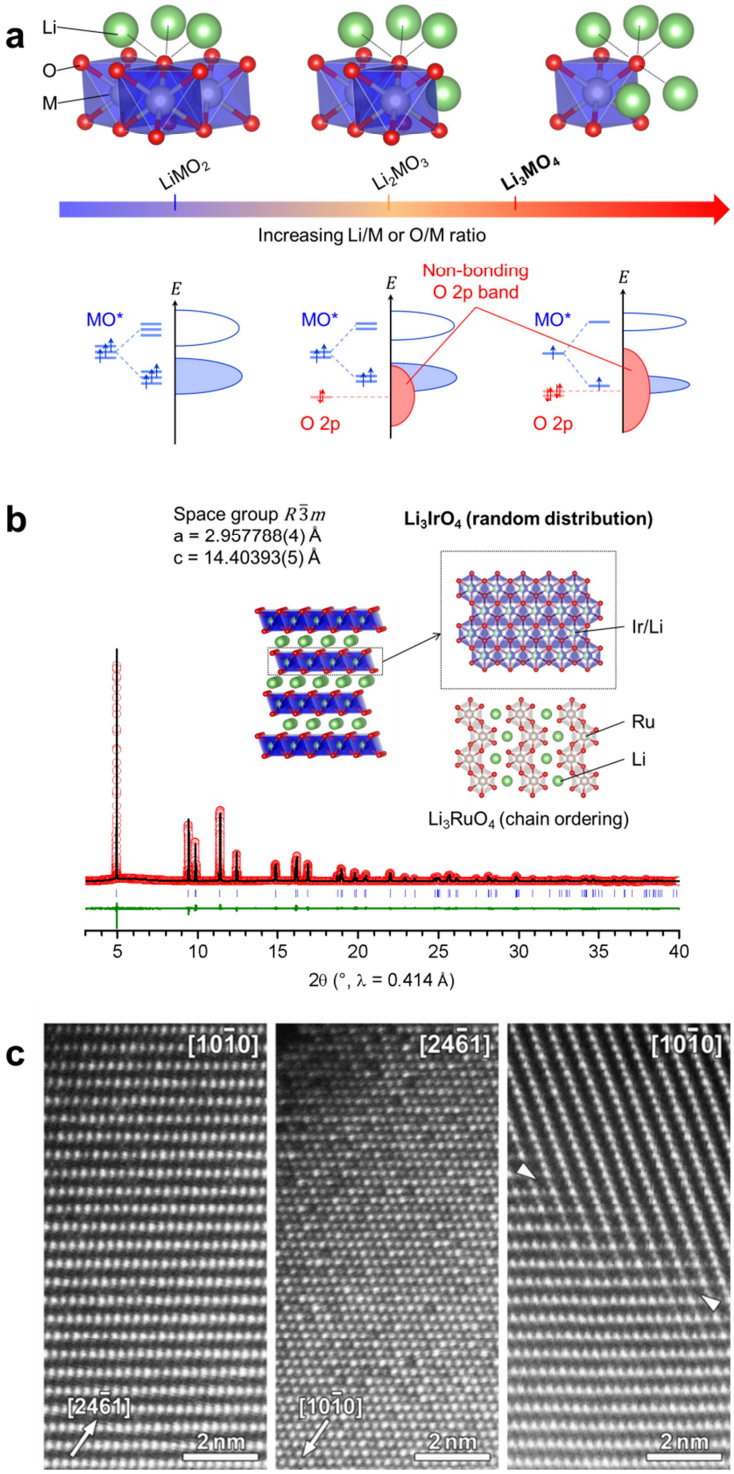

Figure 1: Increasing the O/M ratio from Li_2MO_3 to Li_3MO_4 in rocksalt oxides as a strategy to activate anionic redox. (a) Extra capacity from oxygen redox in Li-rich rocksalt oxides is linked to the presence of non-bonding O(2p) orbitals at the Fermi level. By reducing the number of transition metal coordinating oxygen, it is possible to increase the number of non-bonding O(2p) states at the expense of bonding (MO) and antibonding (MO*) orbitals, thus activating oxygen redox at the expense of cationic redox. (b) Li_3IrO_4 has a

layered structure with no long-range ordering of Li and Ir in the metallic layers. However, on the local scale, it can be expected to be similar to Li_3RuO_4 which forms zig-zag chains of Li and Ru. (c) Typical HAADF-STEM images of Li_3IrO_4 acquired along the $<110>_{NaCl}$ directions of the rock-salt sublattice. The indexes of the directions are given with respect to the hexagonal $R\bar{3}m$ lattice. The images on the left and in the middle confirm layered organization of the structure with random cation distribution in the Li/Ir layers. Image on the right demonstrates coherent intergrowth of structure domains with different orientation and the common plane confined to [24-61] plane (marked with arrowheads).

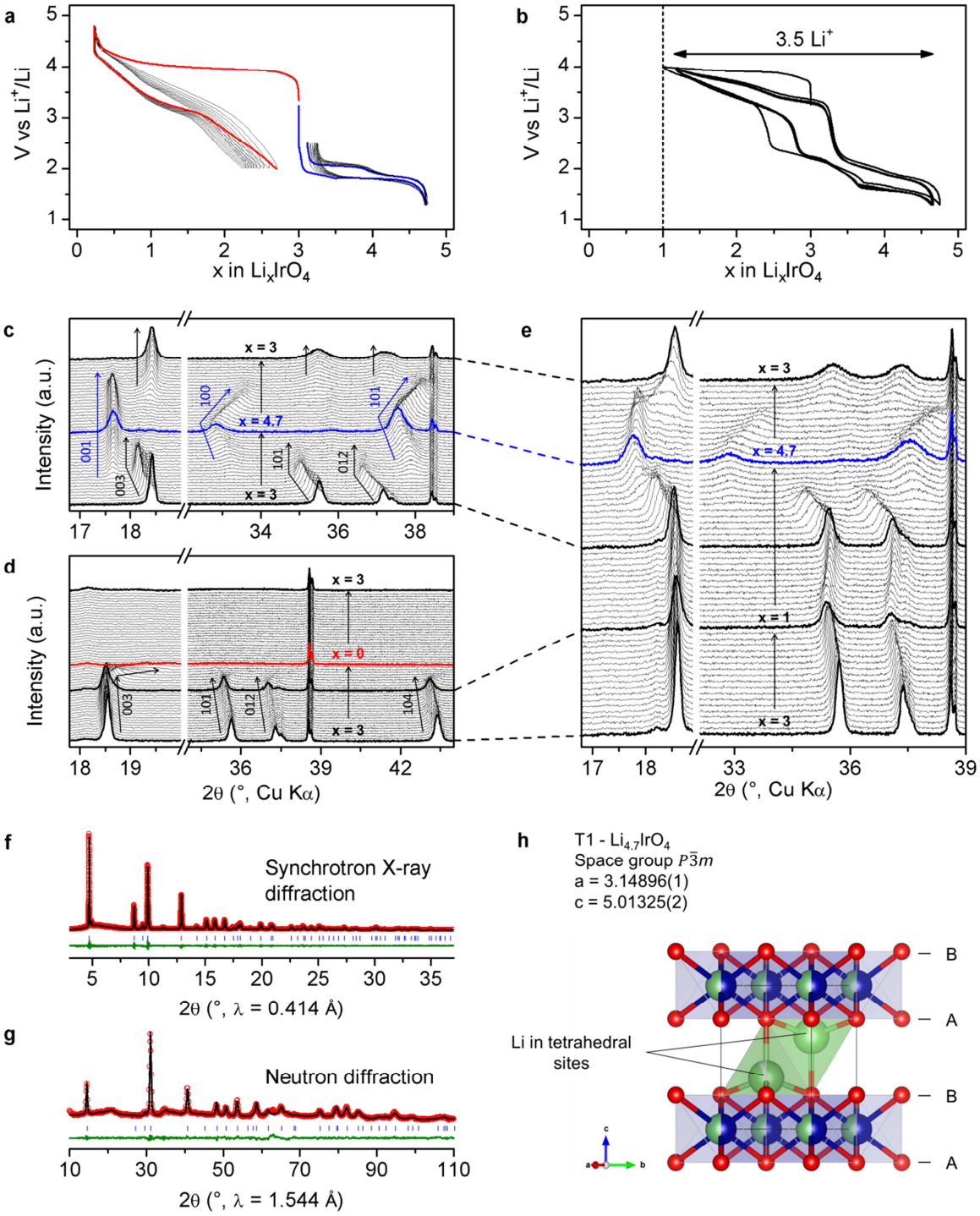

Figure 2: Structural evolution of Li_3IrO_4 upon electrochemical insertion/deinsertion of Li. Galvanostatic curves started on oxidation (red) and reduction (blue) (a). 3 Li can be removed from Li_3IrO_4 and 1.7 extra Li can be inserted in the structure to form $Li_{4.7}IrO_4$. A reversible capacity of 3.5 e^- (340 mAh/g) can be achieved if the delithiation on the first cycle is stopped at x = 1 (b). *In situ* XRD shows that the low voltage process corresponds to a reversible intercalation/deintercalation process, with the formation of a new phase at x = 4.7 (c). The oxidation process comes with an irreversible amorphization of

the material, explaining the modification of the voltage curve after the first charge (d). By stopping the charge at x = 1, *in situ* XRD shows that the structure of the material is preserved, as well as the reversible structural transition observed upon reduction to 1.3 V (e). Rietveld refinement of synchrotron X-ray (f) and neutron (g) diffraction of *ex situ* samples reveal a T1 stacking for $Li_{4.7}IrO_4$ which allows the insertion of extra Li in tetrahedral sites (h).

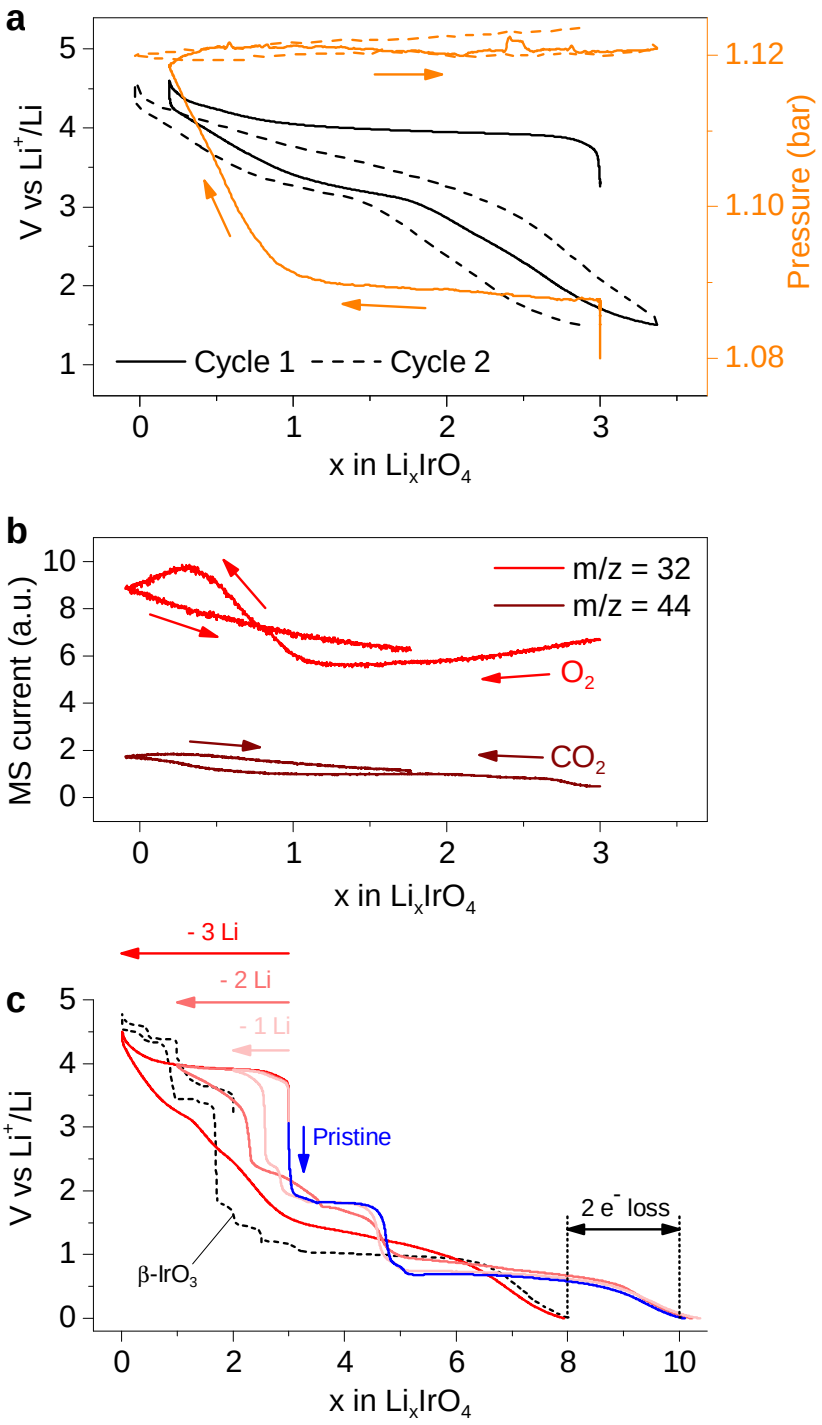

Figure 3: Irreversible capacity loss for total delithiation of Li_3IrO_4. *In situ* pressure measurement during the first two cycles of Li_3IrO_4 on delithiation (a). No significant modification in pressure is observed until the last Li is removed from the structure and the pressure drastically increases. DEMS analysis of the gas formed shows an increased signal of O_2 in the cell, as well as CO_2 to a lesser extent, suggesting that the material loses oxygen below x = 1 (b). The reduction capacity (c) after complete conversion of the material to Ir^0 and Li_2O does not change for the pristine (blue) or after removing one Li or two Li (light

reds). However, almost 2 e^- are lost on reduction when the 3 Li are removed from the structure (red). The reduction capacity of the amorphous phase after losing gas is similar to that of β-IrO_3 (dashed line).

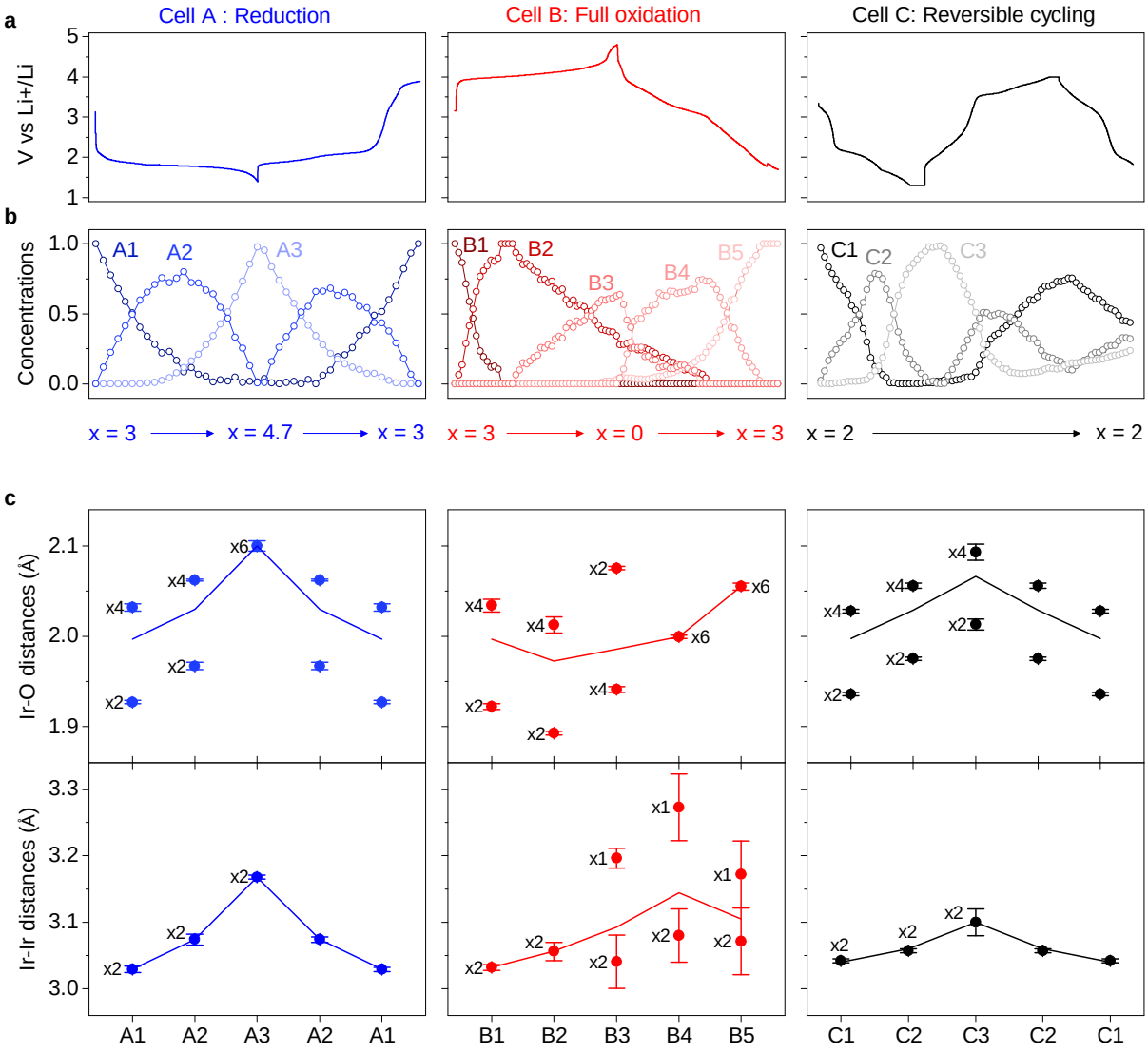

Figure 4: Local structural evolution from *operando* EXAFS analysis at Ir L_{III} edge. Quick-XAS measurements were acquired operando for three cells cycled in different conditions (a). Cell A was started on reduction and cycled between x = 3 and x = 4.7 (left), cell B was fully oxidized to trigger the amorphization before discharging to x = 3 (center) and cell C was charged to x = 1 and partially discharged to x = 2 before the measurement of a full reversible cycle (right). The principal components present in each data sets were extracted using PCA and MCR-ALS analysis as well as their relative concentrations during cycling (b), showing the reversibility (cell A and C) or irreversibility (cell B) of the processes. Fits of the Fourier transform of the EXAFS oscillations extracted at Ir L_{III}-edge (Supplementary Figures 8, 9 and 10) show that the pristine compound has a chain-like ordering of Ir cations at the local scale, similar to Li_3RuO_4, and that during the amorphization process, the connectivity of IrO_6 octahedra increases from 2 to 3. The Ir-O and Ir-Ir bond

lengths obtained from the fits are reported with the multiplicity of each distances indicated next to it (c). Full lines are connecting the average Ir-O and Ir-Ir distances to highlight the distortion of IrO_6 octahedra associated with Ir oxidation/reduction.

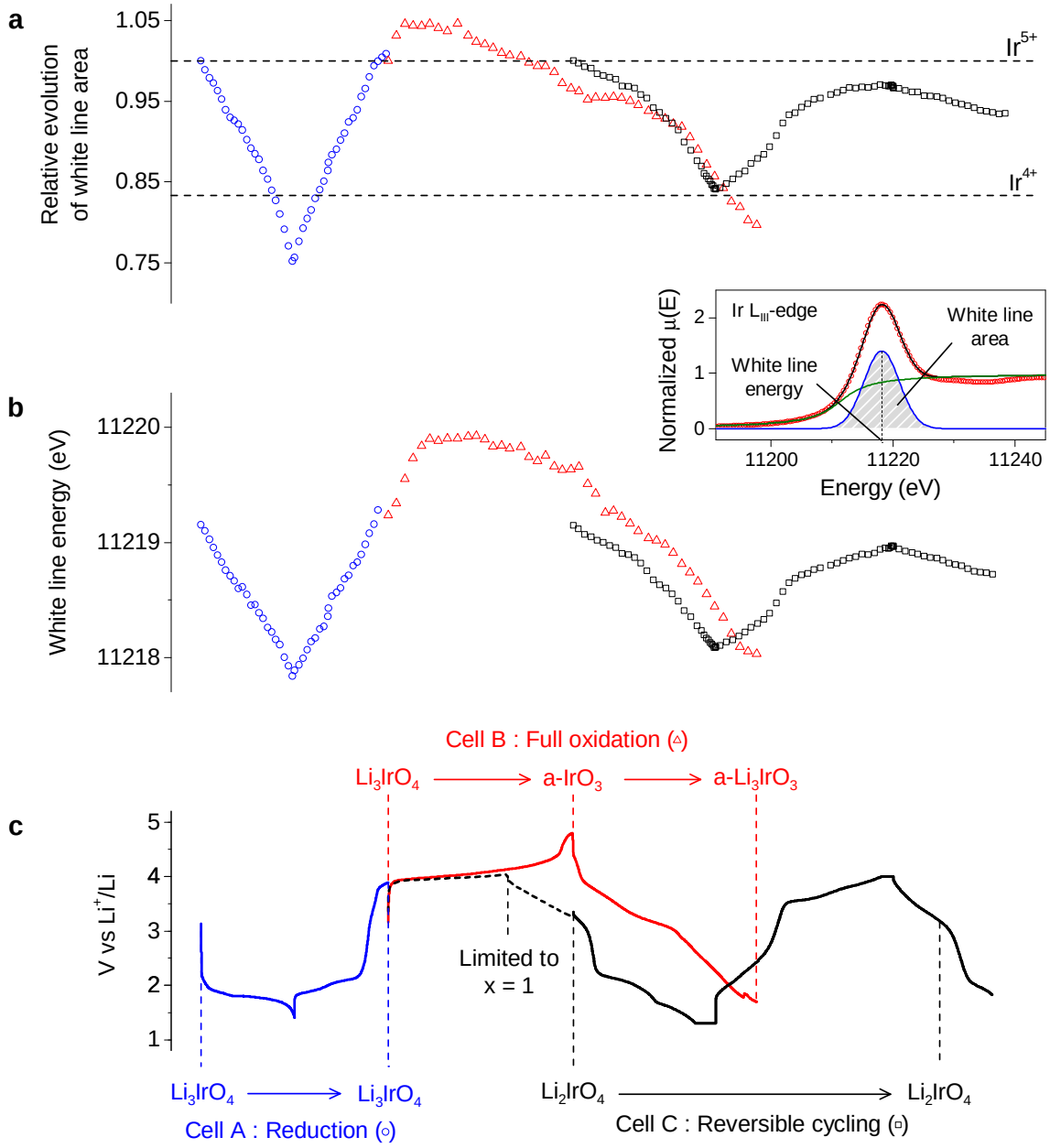

Figure 5: Participation of cationic and anionic redox processes during cycling studied by *operando* XANES. The oxidation state of iridium can be followed by integrating the white line area at the Ir L_{III}-edge which corresponds to the 2p-5d electronic transition (inset). The relative evolution of the WL area (a) is compared to the energy of the white line (b) and reported vs. the composition (c) during cycling for the three cells A (blue circles), B (red triangles) and C (black squares).

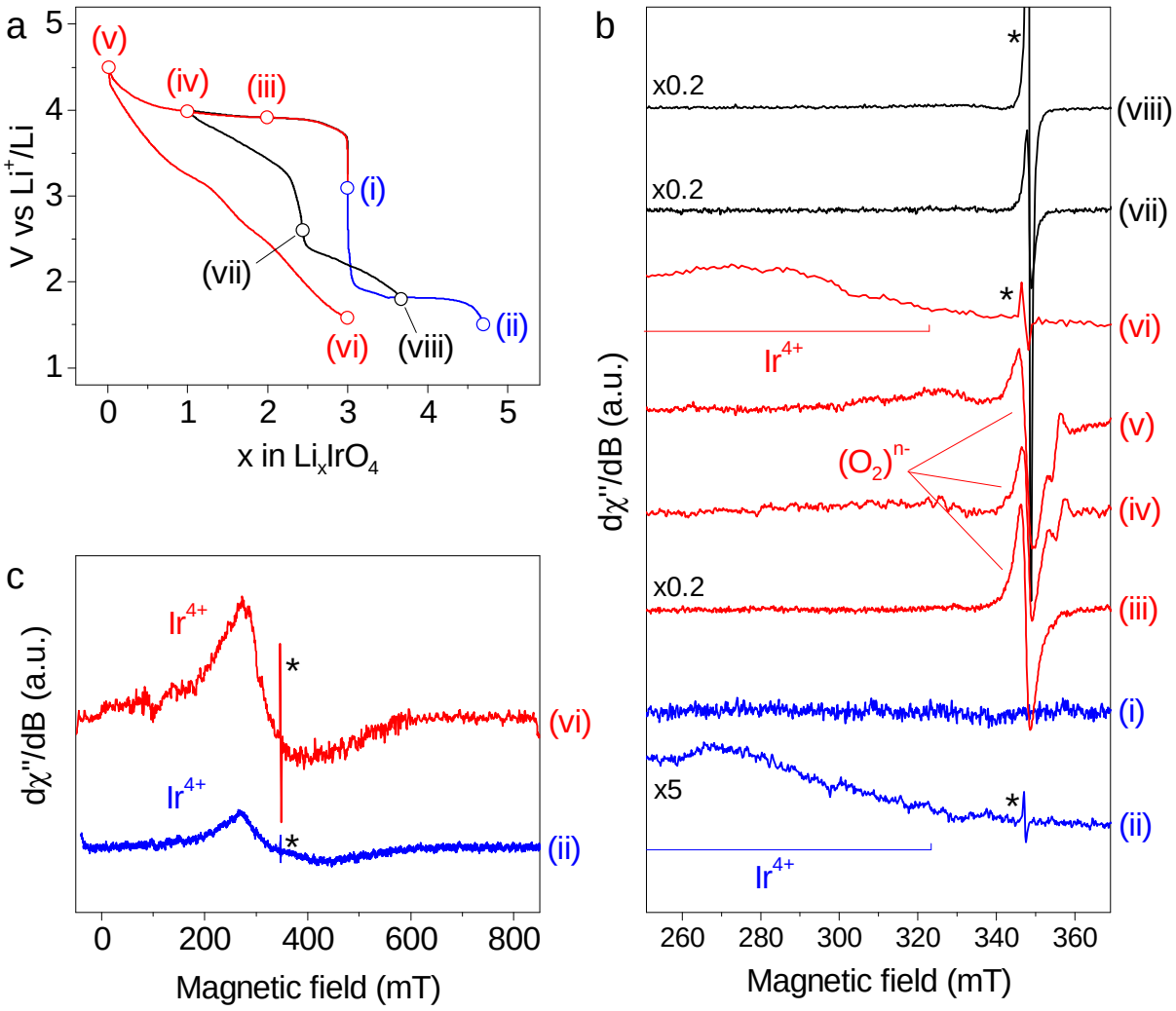

Figure 6: *Ex situ* EPR spectroscopy study of paramagnetic species at different states of charge. No signal is observed for the pristine sample (i). The discharged sample $Li_{4.7}IrO_4$ (ii) shows a very broad signal related to Ir^{4+}. Upon charge (iii - v), an increasingly anisotropic signal of $(O_2)^{n-}$ species is observed. After 1 cycle of charge/discharge (vi), the signal of Ir^{4+} is measured, with a more isotropic shape compared to the signal obtained for the reduced compound (ii). After charging to x = 1 and discharging to 2.6 V (vii), an isotropic signal is measured that still correspond to $(O_2)^{n-}$ and is replaced by the sharp and intense signal of Csp (marked by an asterisk) on further discharge to 1.8 V (viii).